

MIT Open Access Articles

*Al/Fe isomorphic substitution versus
Fe₂O₃ clusters formation in
Fe-doped aluminosilicate nanotubes (imogolite)*

The MIT Faculty has made this article openly available. **Please share**
how this access benefits you. Your story matters.

Citation: Shafia, Ehsan et al. "Al/Fe Isomorphic Substitution versus Fe₂O₃ Clusters Formation in Fe-Doped Aluminosilicate Nanotubes (Imogolite)." Journal of Nanoparticle Research 17.8 (2015): n. pag.

As Published: <http://dx.doi.org/10.1007/s11051-015-3130-2>

Publisher: Springer Netherlands

Persistent URL: <http://hdl.handle.net/1721.1/104627>

Version: Author's final manuscript: final author's manuscript post peer review, without publisher's formatting or copy editing

Terms of Use: Article is made available in accordance with the publisher's policy and may be subject to US copyright law. Please refer to the publisher's site for terms of use.



Al/Fe isomorphic substitution versus Fe₂O₃ clusters formation in Fe-doped aluminosilicate nanotubes (imogolite)

Ehsan Shafia · Serena Esposito · Maela Manzoli · Mario Chiesa ·
Paola Tiberto · Gabriele Barrera · Gabriel Menard · Paolo Allia ·
Francesca S. Freyria · Edoardo Garrone · Barbara Bonelli

Received: 25 May 2015 / Accepted: 21 July 2015 / Published online: 13 August 2015
© Springer Science+Business Media Dordrecht 2015

Abstract Textural, magnetic and spectroscopic properties are reported of Fe-doped aluminosilicate nanotubes (NTs) of the imogolite type, IMO, with nominal composition (OH)₃Al_{2-x}Fe_xO₃SiOH ($x = 0, 0.025, 0.050$). Samples were obtained by either direct synthesis (Fe-0.025-IMO, Fe-0.050-IMO) or post-synthesis loading (Fe-L-IMO). The Fe content was either 1.4 wt% (both Fe-0.050-IMO and Fe-L-IMO) or 0.7 wt% (Fe-0.025-IMO). Textural properties were characterized by High-Resolution Transmission Electron Microscopy, X-ray diffraction and N₂ adsorption/desorption isotherms at 77 K. The presence of different iron species was studied by magnetic moment measurements and three spectroscopies: Mössbauer, UV–Vis and electron paramagnetic

resonance, respectively. Fe³⁺/Al³⁺ isomorphic substitution (IS) at octahedral sites at the external surface of NTs is the main process occurring by direct synthesis at low Fe loadings, giving rise to the formation of isolated high-spin Fe³⁺ sites. Higher loadings give rise, besides IS, to the formation of Fe₂O₃ clusters. IS occurs up to a limit of Al/Fe atomic ratio of ca. 60 (corresponding to $x = 0.032$). A fraction of the magnetism related to NCs is pinned by the surface anisotropy; also, clusters are magnetically interacting with each other. Post-synthesis loading leads to a system rather close to that obtained by direct synthesis, involving both IS and cluster formations. Slightly larger clusters than with direct synthesis samples, however, are formed. The

E. Shafia · P. Allia (✉) · E. Garrone · B. Bonelli (✉)
Department of Applied Science and Technology and
INSTM Unit of Torino-Politecnico, Politecnico di Torino,
Corso Duca degli Abruzzi 24, 10129 Turin, Italy
e-mail: paolo.allia@polito.it

B. Bonelli
e-mail: barbara.bonelli@polito.it

S. Esposito
Department of Civil and Mechanical Engineering,
Università degli Studi di Cassino e del Lazio Meridionale,
Via G. Di Biasio 43, 03043 Cassino, FR, Italy

M. Manzoli · M. Chiesa · G. Barrera
Dipartimento di Chimica and Centro Interdipartimentale
NIS, Università di Torino, Via Giuria 7, 10125 Turin,
Italy

P. Tiberto · G. Barrera
Electromagnetism, I.N.Ri.M., Strada delle Cacce 91,
10135 Turin, Italy

G. Menard
Department of Chemistry and Chemical Biology, Harvard
University, 12 Oxford St., Cambridge, MA 02138, USA

F. S. Freyria
Department of Chemistry, Massachusetts Institute of
Technology, 77 Massachusetts Ave, Cambridge,
MA 02139, USA

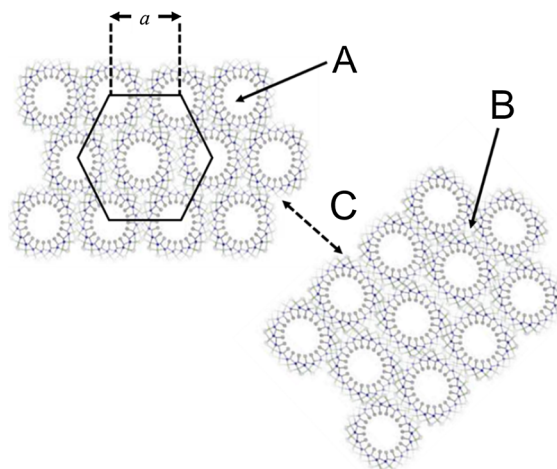
occurrence of IS indicates a facile cleavage/sealing of Al–O–Al bonds: this opens the possibility to exchange Al^{3+} ions in pre-formed IMO NTs, a much simpler procedure compared with direct synthesis.

Keywords Aluminosilicate nanotubes · Imogolite · Isomorphic substitution · High-spin Fe^{3+} sites · Fe_2O_3 clusters · Paramagnetism · Band-gap · Nanocomposites

Introduction

Imogolite (IMO) is a hydrated aluminosilicate with formula $(\text{OH})_3\text{Al}_2\text{O}_3\text{SiOH}$ (Cradwick et al. 1972; Yoshinaga and Aomine 1962) either found in soils (mainly of volcanic origin) or prepared by sol–gel synthesis (Farmer et al. 1983; Farmer and Fraser 1978; Wada et al. 1979). Bridged $\text{Al}(\text{OH})\text{Al}$ groups, with octahedrally coordinated (Oh) Al atoms, occur at the outer surface of aluminosilicate nanotubes (NTs) and non-interacting silanols (SiOH) at the inner surface. The length of a single IMO NT varies between 400 nm and several microns, whereas the inner diameter is constant at 1.0 nm. The outer diameter is ca. 2.0 nm in natural IMO, whereas it varies in the range of 2.5–2.7 nm in the synthetic samples (Cradwick et al. 1972): the presence of different inter-tube impurities may affect NTs packing (Zanzottera et al. 2012) which also depends on the synthesis temperature. The synthesis temperature is usually 373 K, whereas the synthesis at 298 K yields NTs with a radius close to that of natural IMO (Wada 1987).

IMO NTs arrange in bundles with nearly hexagonal packing. This structure gives rise to three kinds of pores (Ackerman et al. 1993; Wilson et al. 2002) shown in Scheme 1: (i) pores A are intra-tube pores, 1.0 nm in diameter, lined by silanols, the related A surface being very hydrophilic and able to interact with probes like H_2O , NH_3 and CO (Bonelli et al. 2009; 2013); (ii) pores B, 0.3–0.4 nm wide, are those among the three aligned NTs within a bundle, hardly accessible even to small molecules, like water (Ackerman et al. 1993; Wilson et al. 2002); (iii) pores C are disordered slit (meso)pores among bundles, the surface of which may interact with larger molecules, like phenol (Bonelli et al. 2009) and 1,3,5-triethylbenzene (Bonelli et al. 2013).



Scheme 1 Three types of pores in IMO: intra-tube pores (A, 1.0-nm diameter); pores among three aligned NTs in a hexagonal packing (B, 0.3–0.4-nm diameter) and slit (meso)-pores among bundles (C)

The interest in IMO-related chemistry has spread recently, one reason being the possibility of allowing changing the compositions of both inner and outer surfaces of NTs. The former can be modified in several ways: (i) by substitution of Si atoms by Ge atoms, giving rise to either single- or double-walled NTs with formula $(\text{OH})_3\text{Al}_2\text{O}_3\text{Si}_{1-x}\text{Ge}_x\text{OH}$ (Mukherjee et al. 2005; Thill et al. 2012); (ii) by grafting organic functionalities at the inner surface of IMO, resulting in $(\text{OH})_3\text{Al}_2\text{O}_3\text{SiO-R}$ NTs, where R is the organic group (Kang et al. 2011); (iii) by properly choosing the Si precursor, to form hybrid NTs with formula $(\text{OH})_3\text{Al}_2\text{O}_3\text{Si-R}$ ($\text{R} = -\text{CH}_3$, $-(\text{CH}_2)_3-\text{NH}_2$) by direct synthesis (Bottero et al. 2011; Kang et al. 2014).

The present work concerns yet another modification of the outer surface, the isomorphic substitution (IS) of Fe^{3+} for Oh Al^{3+} . Although this is a common process in all natural aluminosilicates, little is known about Fe-doped IMO.

The earliest experimental studies on Fe-doped IMO (Ookawa et al. 2006; Ookawa 2012) indicated an upper limit to the amount of iron, in that NTs are preserved up to overall 1.4 wt% Fe content. More recent reports on Fe-doped aluminium-germanate NTs, analogous to IMO NTs, showed that Fe IS is indeed limited to 1.0 wt%, and the formation of Fe oxo-hydroxides unavoidably occurs at higher Fe content (Avellan et al. 2014).

The presence of Fe^{3+} may impart the solid new chemical and solid-state properties. For example,

theoretical calculations envisage that Fe could either isomorphically substitute for Al or create Fe oxo-hydroxide particles, both inside and outside NTs (Alvarez-Ramírez 2009): the presence of Fe species could affect the Fermi level, by reducing the band gap of IMO from 4.7 eV to 2.0–1.4 eV, well into the visible range.

Similarly, no studies are available on the magnetic properties related to the presence of Fe. A vaguely related paper concerns an imogolite-Fe₃O₄ (magnetite) composite, and its behaviour in anion adsorption from polluted water (Arancibia-Miranda et al. 2014).

In the present work, two samples were synthesized with 1.4 wt% Fe content, by adopting either direct (Fe-0.050-IMO) or post-synthesis procedure (Fe-L-IMO). A third sample was obtained, by direct synthesis, with an Fe content corresponding to 0.7 % by weight (Fe-0.025-IMO).

Morphological and textural properties of the three Fe-doped IMO, as measured by means of several techniques, are compared to those of proper IMO. The properties related to the presence of Fe species are studied by means of magnetic moment measurements, Mössbauer, EPR (Electron Paramagnetic Resonance) and UV–Vis spectroscopies.

Experimental

Materials

IMO was obtained as reported elsewhere (Bonelli et al. 2009).

Fe-x-IMO samples were obtained by direct synthesis as follows: in a glove box, an appropriate amount of FeCl₃·6H₂O was added to 20 mM solution of HClO₄, and then TEOS (tetraethoxysilicate) and Al-sec-butoxide were added, with the pH of the resulting mixture being = 4.0. The aqueous mixture was stirred at room temperature for 18 h, diluted to 20 mM in Al, autoclaved at 373 K for 4 days, filtered, washed and dried overnight at 323 K in oven. A reddish-brown powder was obtained, the solution recovered by filtration being instead transparent.

Fe-L-IMO was prepared by adding appropriate amounts of IMO and FeCl₃·6H₂O into water (resulting pH = 4.0) for 24 h under stirring and finally adding NH₄OH solution (33 % by weight) to precipitate all

Fe³⁺ as oxo/hydroxide species. The solid was then filtered, washed and dried in oven at 323 K overnight. Chemical analysis of the supernatant solution did not detect the presence of residual iron with all the Fe-doped samples.

Methods

Electron micrographs were obtained on a high-resolution transmission electron microscope (HRTEM, Jeol 3010-UHR) operating at 300 kV, equipped with a LaB₆ filament and an Oxford Inca Energy TEM 300 EDS X-ray analyser (Oxford Link) for atomic recognition. Digital micrographs were acquired by a (2 k × 2 k)-pixel Ultrascan 1000 CCD camera and processed by Gatan digital micrograph. Before HRTEM measurements, the powder samples were milled in an agate mortar and deposited on a copper grid covered with a lacey carbon film.

Powder X-ray diffraction (XRD) patterns were obtained on a X'Pert Phillips diffractometer operating with Cu Kα radiation (1.541874 Å) in the 2.5–18° 2θ range (step width = 0.02°, time per step: 2.00 s).

To determine Brunauer–Emmett–Teller specific surface area (BET SSA) and porous volume values reported in Table 1, N₂ isotherms were measured at 77 K on samples previously outgassed at 523 K, in order to remove water and other atmospheric contaminants, still preserving NT structure (MacKenzie et al. 1989; Zanzottera et al. 2012). Non-local density functional theory method (NL-DFT) was used to determine pores size distributions (PSDs), by means of an N₂-silica kernel for cylindrical pores.

Room-temperature magnetization curves were measured by means of an ultrasensitive alternating-gradient field magnetometer (AGFM; sensitivity 1 × 10^{−8} emu) operating in the magnetic field range −18 kOe < H < 18 kOe and equipped with a sample-holder suitable for measurements on magnetically diluted systems such as the present IMO NTs. The magnetic response of the sample holder was measured and subtracted from the data in order to get rid of spurious magnetic effects from the measuring setup.

The zero-field ⁵⁷Fe Mössbauer spectra were measured with a constant acceleration spectrometer (SEE Co, Minneapolis, MN). The Fe-containing samples (ca. 50 mg) were prepared as Paratone-N mulls and frozen in liquid nitrogen prior to insertion into the spectrometer. Isomer shifts are quoted relative to Fe

Table 1 Samples textural properties as derived by N₂ sorption isotherms at 77 K and low angles XRD patterns

Sample	Fe wt%	BET SSA (m ² g ⁻¹)	Pore Total volume (cm ³ g ⁻¹)	Micro-pore ^a Volume (cm ³ g ⁻¹)	d ₁₀₀ (nm) (±0.01)	a (nm)
IMO	–	383	0.21	0.13	2.27	2.62
Fe-L-IMO	1.4	400	0.27	0.13	2.27	2.62
Fe-0.025-IMO	0.7	450	0.22	0.15	2.17	2.51
Fe-0.050-IMO	1.4	455	0.22	0.14	2.17	2.51

Cell parameter, *a*, as calculated by applying the eq. $a = 2d_{100}/\sqrt{3}$

^a As obtained by applying the *t*-plot method

metal at 296 K. Data were acquired at 90 K and processed, simulated, and analysed using an in-house package for IGOR Pro 6 (Wavemetrics, Lake Oswego, OR).

Diffuse reflectance (DR) UV–Vis spectra of samples outgassed at 523 K were measured on a Cary 5000 UV–Vis–NIR spectrophotometer (Varian instruments).

EPR spectra were recorded at 77 K on a Bruker EMX spectrometer operating at X-band frequency (9.78 GHz) and equipped with a cylindrical cavity operating at a 100-kHz field modulation. A modulation amplitude of 0.3 mT was used, and the microwave power was adjusted to prevent saturation of the spin systems.

Results and discussion

Textural and morphological properties

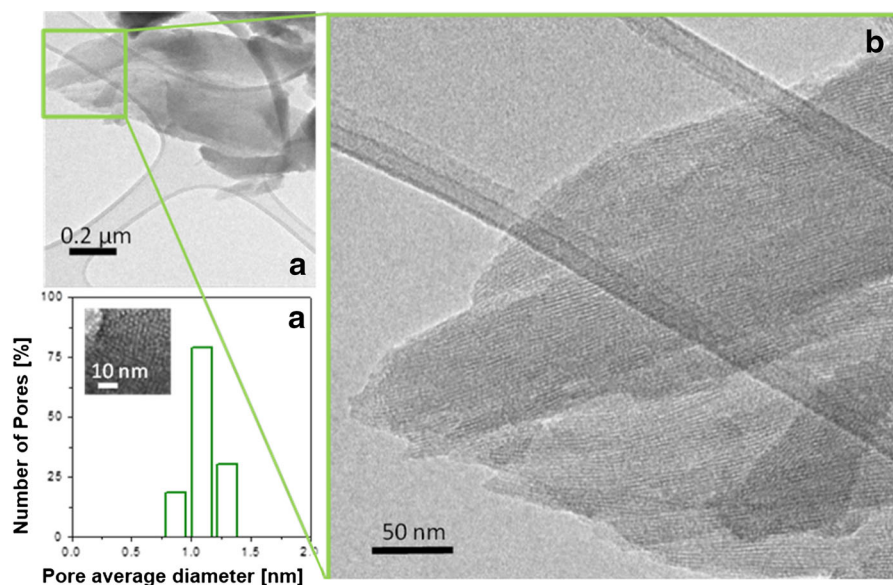
A thorough TEM characterization was carried out on all samples. Figure 1 shows selected images collected on IMO at different magnifications, concerning, respectively, a whole particle (section a), a bundle with parallel NTs (section b), and a detail of a bundle termination, showing a hexagonal array of NTs (section c). The morphological features of bare IMO are maintained, independently of both Fe amount and synthesis procedure (Fig. 2a, d, f, h). Fe is homogeneously distributed, as shown by the EDS maps (Fig. 2c, g, i), demonstrating the effectiveness of both synthesis procedures. Some Fe-containing clusters at the outer surface of NTs were observed, especially evident with Fe-L-IMO (arrows in Fig. 2h). Their sizes were evaluated on both Fe-0.050-IMO and Fe-L-IMO

by considering electron micrographs acquired at 50,000 magnification. The PSDs in Fig. 2l were obtained by considering 450 particles: Fe-0.050-IMO has smaller clusters, whereas the loading procedure leads to larger ones in Fe-L-IMO; accordingly, the average particle diameters (calculated as $d_m = \sum d_i n_i / \sum n_i$, where n_i is the number of particles of diameter d_i) result as 4.0 and 4.4 nm for Fe-0.050-IMO and Fe-L-IMO, respectively.

The NTs spatial arrangement may be appreciated also in Fig. 3, reporting XRD patterns of IMO, Fe-0.025-IMO, Fe-0.050-IMO, and Fe-L-IMO, all corresponding to hexagonal packing of NTs being clearly visible in Fig. 1. The d_{100} diffraction is at $2\theta = 3.88^\circ$ with both IMO and Fe-L-IMO (vertical bar), and at slightly higher 2θ values with both Fe-0.025-IMO ($2\theta = 4.03^\circ$) and Fe-0.050-IMO ($2\theta = 4.06^\circ$). The cell parameter *a* (i.e. the distance between two aligned NTs, Scheme 1) is 2.62 nm with both IMO and Fe-L-IMO (Table 1), and 2.51 nm with both Fe-x-IMO samples. Upon performing Fe³⁺/Al³⁺ IS, NTs inner diameter should increase, as the evidence reported below indicates the occurrence of isolated Oh Fe³⁺ species in high-spin state, which have a Shannon radius of 0.645 Å definitely larger than Oh Al³⁺ (0.535 Å).

N₂ adsorption isotherms in Fig. 4a show the features expected for microporous systems with some mesoporosity (Table 1). Note that Fe-L-IMO has larger mesopores volume, because the loading procedure mainly affects the C surface. In agreement with the idea that Fe³⁺/Al³⁺ IS should increase the diameter of NTs, PSDs curves in section b of the figure show a slight increase of the A pores diameter in the sequence IMO = Fe-L-IMO < Fe-0.025-IMO < Fe-0.050-IMO. However, other factors could lead to

Fig. 1 TEM images of an IMO bundle (a), formed by parallel NTs (b) that are organized into a hexagonal array (c). Instrumental magnification: $\times 10000$ in section a; $\times 50000$ in section b



NTs with different diameters, like the fact that each circumference in Fe-doped IMO could contain a different number of units with respect to proper IMO, for which a minimum strain energy was calculated for NTs with 12 units in the circumference (Konduri et al. 2006). Further support to the observed trend comes, however, from HRTEM pictures: internal pore diameter, as carefully measured on IMO and Fe-x-IMO samples, showed an increase in the series IMO (1.05 nm) < Fe-0.025-IMO (1.29 nm) < Fe-0.050-IMO (1.34 nm) (Figs. 1b, 2c, e). The two adopted methods for evaluation of pore diameters gave comparable results and so, although absolute values are not entirely worthy of trust, the trend is most probably reliable.

The smaller a value for Fe-containing samples, as opposed to the probably larger internal diameter, could be due to the presence, in the inter-tube spaces, of anions coming from the synthesis bath, joining adjacent NTs although not being part of the IMO formula. With IMO, previous work (Zanzottera et al. 2012) has indeed shown the occlusion of some perchlorate anions coming from the synthesis batch, since molecular oxygen was released at high temperature during TG-mass analysis (Zanzottera et al. 2012). During the synthesis of Fe-x-IMO, chloride ions likely replace (larger) perchlorate anions, thereby decreasing the final a value. Accordingly, thermal

treatment of both Fe-x-IMO samples did not show any release of oxygen, as measured by TG-Mass analysis (not reported). Nonetheless, Amara et al. have shown that hexagonalization of NTs' shape occurs, a process also leading to smaller a values (Amara et al. 2014). Although the latter process was observed with aluminium-germanate NTs, i.e. imogolite-like materials with different chemical composition and structural features including NTs' pore size and length, the aforementioned hypothesis may not be completely disregarded, in that the presence of Fe could be able to affect NTs' mechanical properties and deformation.

Effects of the presence of Fe on magnetic and spectroscopic properties

Isothermal magnetization curves of the samples at room temperature are reported in Fig. 5. IMO exhibits a pure diamagnetic behaviour; instead, Fe-x-IMO and Fe-L-IMO samples display a paramagnetic-like response. To single out the contribution from Fe ions, the magnetization of IMO has been subtracted from that of Fe-doped samples. Resulting $M(H)$ curves (Fig. 6) confirm that Fe-0.025-IMO is nearly perfectly paramagnetic; a more complex behaviour, where a sigmoidal, anhysteretic magnetic signal is superimposed to a paramagnetic response, is observed with

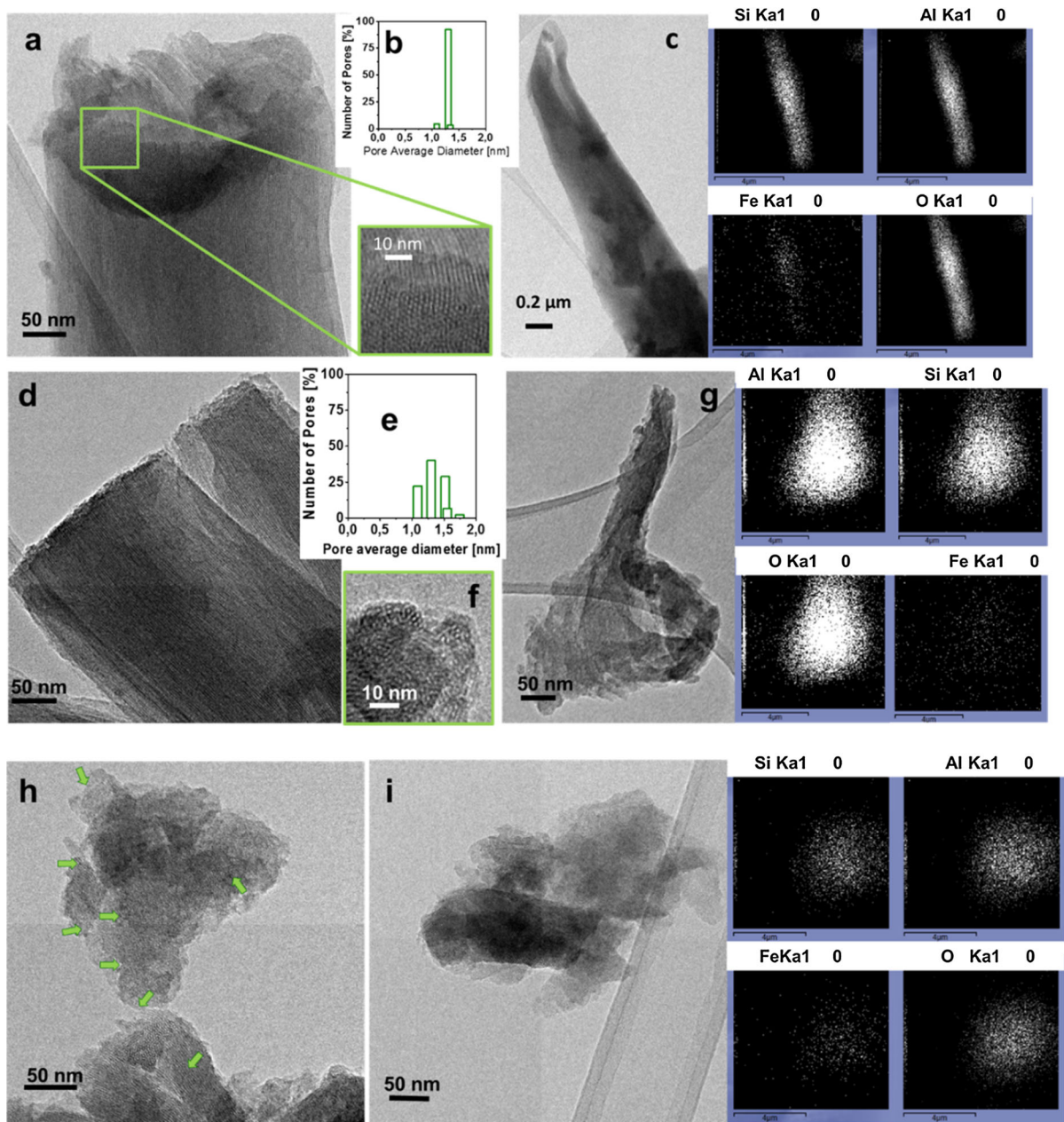


Fig. 2 TEM images of Fe-0.025-IMO, Fe-0.050-IMO and Fe-L-IMO formed by parallel NTs (sections **a**, **d** and **h**, respectively) into a hexagonal array (zoom of section **a**, sections **f** and **h**). Sections **b** and **e**: pore size distributions of Fe-0.025-IMO and Fe-0.050-IMO, respectively. Sections **c**, **g** and **i**: Fe-0.025-IMO, Fe-0.050-IMO and Fe-L-IMO bundles and

corresponding EDS maps allowing the speciation of Si, Al, Fe and O elements. Section **i**: particles size distribution of Fe_2O_3 clusters observed with Fe-L-IMO and Fe-0.050-IMO. Instrumental magnifications: $\times 10000$ (section **a**), $\times 40000$ (section **g**) and $\times 50000$ (other sections)

both Fe-0.050-IMO and Fe-L-IMO, with the signal from Fe-0.050-IMO being weaker (inset of Fig. 6). The sigmoidal components in Fig. 7 have been singled

out by subtracting the paramagnetic-like signal (estimated by fitting the high-field slope of the $M(H)$ curves).

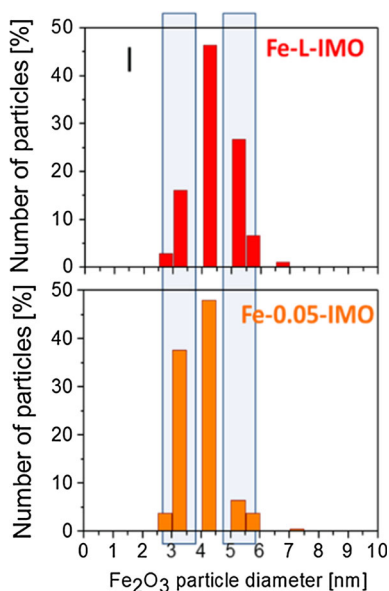


Fig. 2 continued

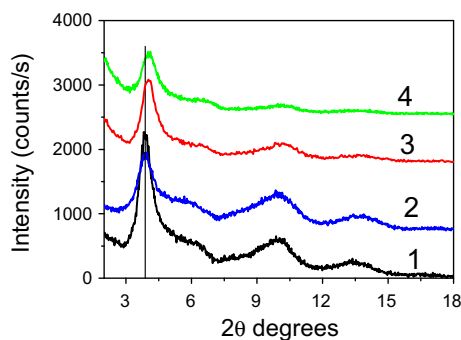


Fig. 3 Low-angle XRD patterns of the following powder samples: IMO (1), Fe-L-IMO (2), Fe-0.025-IMO (3) and Fe-0.050-IMO (4)

The nominal composition yield theoretical number N of Fe ions per gram of substance as $N = 7.55 \times 10^{19}$ ions/g for Fe-0.025-IMO and $N = 1.51 \times 10^{20}$ ions/g for both Fe-0.050-IMO and Fe-L-IMO. According to the simplest model, the magnetic susceptibility of a Van Vleck's paramagnet is $\chi_{\text{para}} = \frac{Ng_J^2 \mu_B^2 S(S+1)}{3k_B T}$, where T is the measurement temperature, μ_B is the Bohr magneton, and k_B is the Boltzmann's constant (Coey 2009). For isolated Fe^{3+} ions, the ionic Landé factor $g_J = 2$ (the g_J factor used here is different from the electronic g_{eff} factor as determined by EPR measurements, vide infra) and $S = 5/2$ according to Hund's rules. At $T = 293$ K, the predicted values for

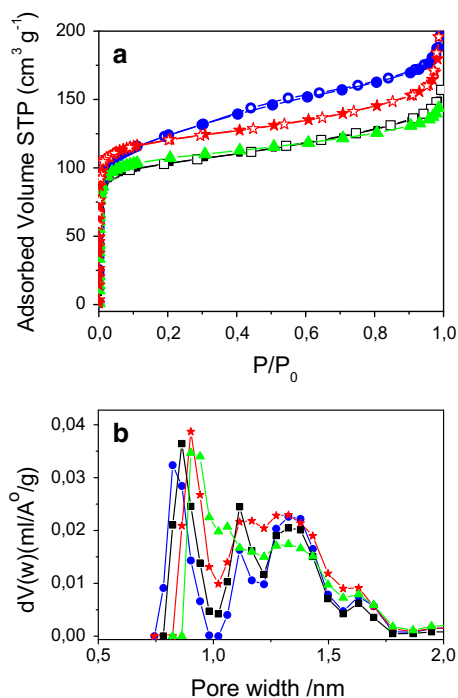


Fig. 4 Section **a**: N_2 sorption isotherms at 77 K of IMO (squares), Fe-L-IMO (circles), Fe-0.025-IMO (stars) and Fe-0.050-IMO (triangles) samples dehydrated at 523 K. Full and hollow symbols refer to adsorption and desorption branches, respectively. Section **b**: Pore size distributions of IMO (squares), Fe-L-IMO (circles), Fe-0.025-IMO (stars) and Fe-0.050-IMO (triangles) as obtained by applying the NL-DFT method

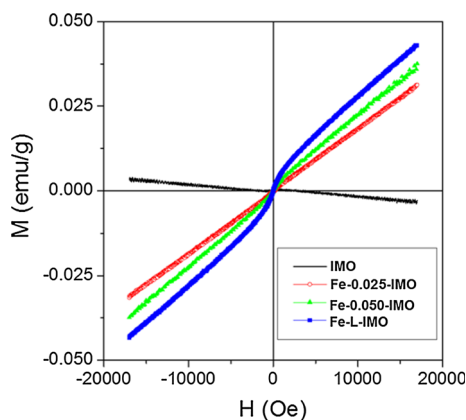


Fig. 5 Room-temperature magnetization curves of IMO and Fe-doped IMO after subtraction of the magnetic response of the experimental setup

the magnetic susceptibility are $\chi_{\text{para}} = 1.87 \times 10^{-6}$ emu $\text{g}^{-1}\text{Oe}^{-1}$ in Fe-0.025-IMO; and $\chi_{\text{para}} = 3.75 \times 10^{-6}$ emu $\text{g}^{-1}\text{Oe}^{-1}$ in both Fe-0.050-IMO

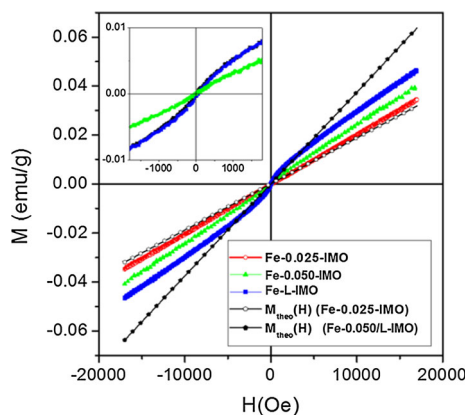


Fig. 6 The same as in Fig. 5 for Fe-doped IMO after subtraction of the diamagnetic response from IMO. Inset: magnified low-field curves of Fe-0.050-IMO and Fe-L-IMO samples

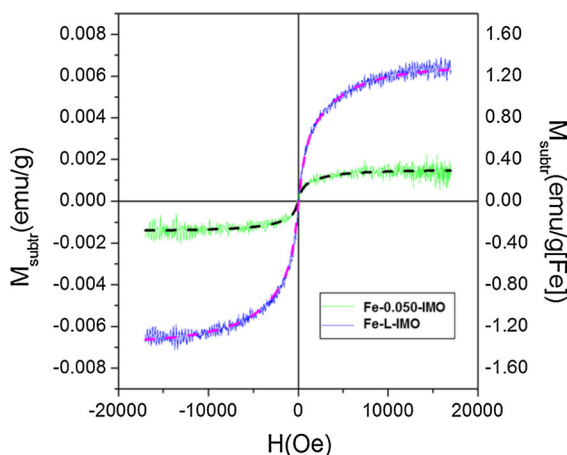


Fig. 7 Magnetic contribution from the surface of hematite nanoclusters in Fe-0.050-IMO and Fe-L-IMO. *Left-side vertical scale* magnetization per gram of material; *right-side vertical scale* magnetization per gram of Fe contained in the Fe_2O_3 clusters. *Dashed lines* curve-fits of the experimental results to superparamagnetic Langevin functions

and Fe-L-IMO. The straight lines $M_{\text{theo}}(H)$ obtained by using these two values of χ_{para} are reported in Fig. 6 (open and full symbols, respectively). With both Fe-0.050-IMO and Fe-L-IMO, the measured curves deviate from the straight-line behaviour around the origin, reflecting the contribution of the sigmoidal magnetic component singled out in Fig. 7. Instead, a notable agreement between the theoretical prediction and the experimental curve is found for Fe-0.025-IMO: the extremely slight discrepancy from linearity

suggests the presence of a vanishingly small sigmoidal component, the presence of which will be neglected here, although EPR measurements reported below give some support to the presence of such a component. The overall indication is that in Fe-0.025-IMO most Fe introduced by direct synthesis is in the form of substitutional, basically non-interacting high-spin Fe^{3+} ions.

In both Fe-0.050-IMO and Fe-L-IMO samples, the prediction for the Van Vleck's paramagnetic susceptibility leads, instead, to a theoretical line with a definitely higher slope than the one actually measured. The sigmoidal curves obtained by subtraction (Fig. 7) reveal the occurrence of non-isolated Fe^{3+} ions in magnetic nanoparticles, in agreement with TEM analysis, indicating the presence of Fe_2O_3 clusters. Their magnetic response is compatible with both hematite ($\alpha\text{-Fe}_2\text{O}_3$) and maghemite ($\gamma\text{-Fe}_2\text{O}_3$) structure. Hematite exhibits an anti-ferromagnetic behaviour below the Morin temperature (Chikazumi 1997) and becomes a weak ferromagnet above it; the transition occurs well below room temperature in bulk hematite and at even lower temperatures in nanoparticles (Eid et al. 2011); consequently, hematite nanoparticles possibly present in these samples should exhibit a weak ferromagnetic signal at room temperature. A closely similar signal should arise also from maghemite nanoparticles, because $\gamma\text{-Fe}_2\text{O}_3$ is ferri-magnetic (Chikazumi 1997).

Since the clusters observed by TEM are small ($d_m \cong 4.0\text{--}4.4$ nm) and characterized by a very high surface-to-volume ratio, it can be presumed that the actual distribution of magnetic moment directions in each nanoparticle is dominated by strong, site-dependent surface anisotropy (Zysler et al. 2005), basically resulting in a highly disordered, spin-glass-like arrangement of magnetic moments (Kodama et al. 1996). In this case, the magnetic moments are extremely correlated and are predicted to be quite insensitive to an applied magnetic field having maximum amplitude comparable to the one used in the present measurements. This picture would actually apply to both hematite and maghemite clusters.

The relative amount of Fe ions in the two main phases (substitutional Fe^{3+} ions and $\alpha/\gamma\text{-Fe}_2\text{O}_3$ clusters) evidenced by susceptibility measurements can be estimated by comparing the actual slopes of the $M(H)$ curves with the theoretical predictions for the nominal concentrations. The experimental numbers of

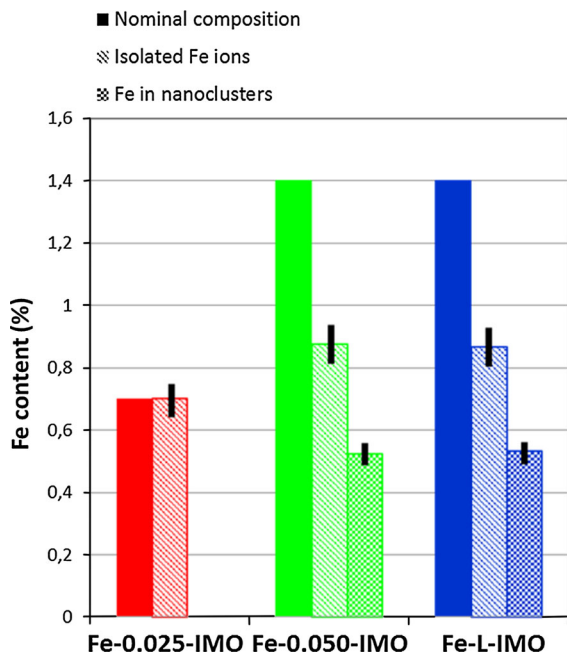


Fig. 8 Iron content (expressed in wt% of the samples) in the form of isolated Fe^{3+} ions and hematite nanoclusters for all examined samples. The nominal Fe content is shown for comparison

Fe^{3+} ions in the pure paramagnetic phase turn out to be $N_{\text{exp}} = 9.35 \times 10^{19}$ ions g^{-1} in Fe-0.050-IMO and $N_{\text{exp}} = 9.46 \times 10^{19}$ ions g^{-1} in Fe-L-IMO. These values can be transformed into percentages, shown along with the nominal Fe concentrations in Fig. 8. In Fe-L-IMO, the estimated number of Fe ions in the Fe_2O_3 clusters turns out to be $(N - N_{\text{exp}}) = 5.64 \times 10^{19}$ ions g^{-1} (per gram of material), corresponding to a fraction $f = 0.374$ of the total Fe mass introduced in the material; therefore, the mass of Fe in clusters is 5.23×10^{-3} g (per gram of material). With Fe-0.050-IMO, a very similar value of the mass of Fe in clusters is found (5.33×10^{-3} g per gram of material).

The magnetization curves shown in Fig. 7 can therefore be expressed per gram of Fe in Fe_2O_3 clusters ($\text{emu/g}[\text{Fe}]$; right-side axis). It may be noted that the estimated maximum magnetization values from Fe_2O_3 clusters in both Fe-0.050-IMO and Fe-L-IMO (corresponding to perfect alignment of all spins on the magnetic sites) are $M_{\text{max}} = (N - N_{\text{exp}}) g_J [S(S + 1)]^{1/2}$; $\mu_B \cong 3.2 \text{ emu/g}[\text{Fe}]$ and $3.1 \text{ emu/g}[\text{Fe}]$ respectively, i.e. almost more than twice the high-field value of $M(H)$ measured in Fe-L-IMO and

about eight times higher than that in Fe-0.050-IMO (Fig. 7).

This result can be explained by considering that in the explored interval of magnetic field values the magnetic moments of clusters are most effectively pinned by surface anisotropy and do not substantially contribute to the $M(H)$ curve. The smaller sigmoidal signal observed in Fe-0.050-IMO could indicate either a more efficient anisotropy pinning of magnetic moments, and therefore a smaller average size of the Fe_2O_3 clusters, or a larger fraction of weak-ferromagnetic $\alpha\text{-Fe}_2\text{O}_3$ with respect to ferrimagnetic $\gamma\text{-Fe}_2\text{O}_3$, as in this case, a lower amplitude of the sigmoidal curve is expected. An ultimate choice between the two hypothesis is not possible on the basis of the present measurements, but the particles size distribution in Fig. 21 show that in Fe-0.050-IMO, smaller clusters do occur.

Finally, both experimental curves in Fig. 7 are well fitted by superparamagnetic Langevin functions (dashed lines in Fig. 7) providing the values of 7.7×10^{-17} emu in Fe-L-IMO and 11.8×10^{-17} emu in Fe-0.05-IMO for the magnetic moments associated to a single ordering magnetic unit. Considering the magnetic moment per unit formula of maghemite ($2.5 \mu_B$) and an average Fe_2O_3 cluster volume ($V \cong 4.5 \times 10^{-20}$ emu), one expects a mean magnetic moment of about $2080 \mu_B \cong 1.9 \times 10^{-17}$ emu on every single Fe_2O_3 cluster. A closely similar value is expected for hematite clusters. The results for the magnetic moment per ordering magnetic unit obtained by the Langevin-curve fits indicate that the magnetic units coherently responding to an external magnetic field are not single Fe_2O_3 clusters, but small, magnetically aggregate ensembles comprising some neighbouring clusters (ca. 4–6). The existence of a certain degree of magnetic correlation among Fe_2O_3 clusters is to be expected indeed, because of the small intercluster distances shown in Figs. 1 and 2 with ensuing non-negligible magnetic dipolar interaction. Moreover, a larger value is found with Fe-0.050-IMO, in which smaller clusters occur, indicating that the actual magnetic object is an ensemble of clusters rather than a single one and that the ensemble for Fe-L-IMO is different from that of Fe-0.050-IMO.

The zero-field ^{57}Fe Mössbauer spectra of Fe-containing IMO are shown in Fig. 9, all featuring very similar single quadrupole doublets. Both Fe-L-IMO and Fe-0.025-IMO samples have identical

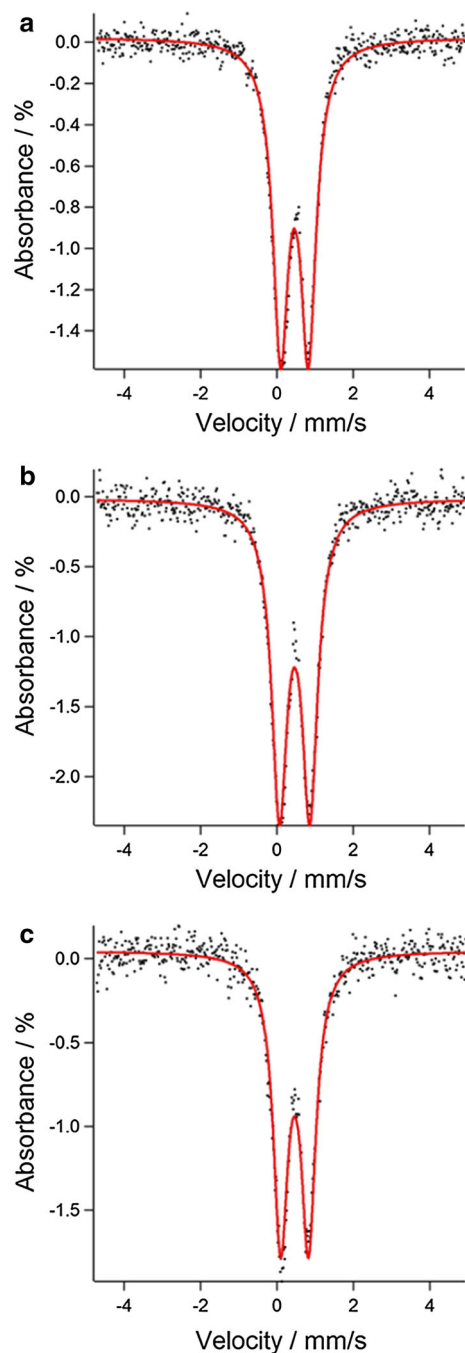


Fig. 9 Zero-field ^{57}Fe Mössbauer spectra at 90 K. Solid red line represents the fit to the data and yields the following parameters: **a** for Fe-L-IMO, $\delta = 0.46$ mm/s; $|\Delta E_Q| = 0.73$ mm/s; **b** for Fe-0.050-IMO, $\delta = 0.46$ mm/s; $|\Delta E_Q| = 0.80$ mm/s and **c** for sample Fe-0.025-IMO, $\delta = 0.46$ mm/s; $|\Delta E_Q| = 0.73$ mm/s. (Color figure online)

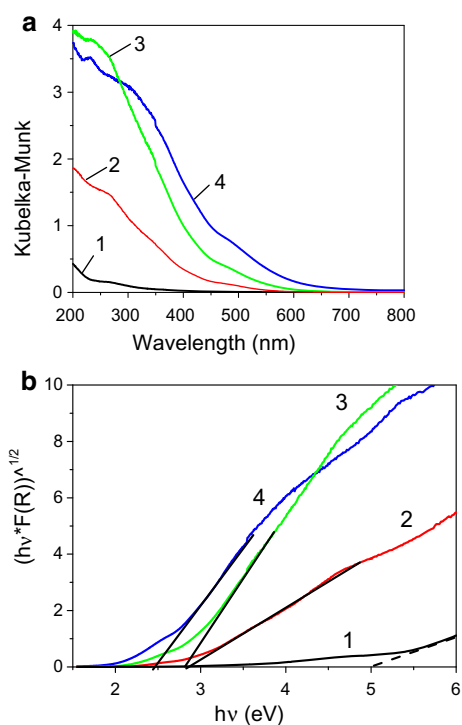
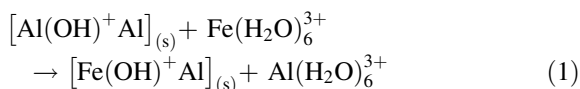


Fig. 10 Section **a**: DR UV-Vis spectra of IMO (1), Fe-0.025-IMO (2), Fe-0.050-IMO (3) and Fe-L-IMO (4). Section **b**: corresponding Tauc's plot

isomer shift (δ) and quadrupole splitting ($|\Delta E_Q|$) values (δ , $|\Delta E_Q|$ (mm/s): 0.46, 0.73, Fig. 9a, c, respectively), whereas Fe-0.050-IMO has a slightly larger quadrupole splitting value (δ , $|\Delta E_Q|$ (mm/s): 0.46, 0.80, Fig. 9b). These data are consistent in all cases with Fe centres in the 3+ oxidation state (Fallet et al. 2003; Lopez et al. 2002; Papaefthymiou et al. 2002; Reis et al. 2003), ruling out the presence of Fe^{2+} in agreement with the synthesis conditions. As expected, with IMO, no Fe centres were detected by ^{57}Fe Mössbauer spectroscopy (spectrum not reported).

DR UV-Vis spectra of dehydrated samples are reported in Fig. 10: IMO has, as expected, a negligible absorption in the UV-Vis region (curve 1), whereas the Fe-doped samples show similar, though not equal, UV-Vis features. Both Fe-x-IMO samples (curves 2 and 3) strongly absorb at 270 nm, and show a minor absorption band at 480 nm, almost negligible with Fe-0.025-IMO, in agreement with magnetic measurements. According to the literature, the former signal is

due to charge-transfer transitions (CT) from O^{2-} to isolated Oh Fe^{3+} ions, with the latter being due to d–d transitions of Fe^{3+} in Fe_2O_3 nanoclusters (Borghi et al. 2010; Wang et al. 2002). Fe-L-IMO spectrum (curve 4) is similar to that of Fe-0.050-IMO, although slightly shifted to higher wavelengths, with a component at 310 nm and more intense d–d transitions. The component at 310 nm is assigned to CT transitions in iron oxide clusters (Borghi et al. 2010); UV–Vis spectra point out the preferential formation of Fe_2O_3 clusters by post-synthesis method, although Fe-L-IMO also absorbs at 270 nm. At 1.4 wt% Fe content, both isolated Oh Fe^{3+} species and aggregated Fe–O–Fe groups are obtained, the latter being more abundant with Fe-L-IMO. The presence of isolated Oh Fe^{3+} sites in Fe-L-IMO indicates that ionic exchange also occurred between structural Al^{3+} and Fe^{3+} ions in water:



On the other hand, the occurrence of some Fe_2O_3 clusters in Fe-x-IMO indicates that the actual isomorphic substitution of Fe for Al in the IMO structure is lower than that corresponding to 1.4 % by weight, in agreement with magnetic data measurements.

To get an insight into the electronic nature of the synthesised solids, the spectra in Fig. 10 were processed according to Tauc's formula, allowing the evaluation of the band gap (E_g). Corresponding plots

are reported in Fig. 10b: IMO has an E_g of 4.9 eV, in fair agreement with the value of 4.6 eV obtained by theoretical calculations (Alvarez-Ramírez 2009). In the only presence of substitutional Fe^{3+} ions (Fe-0.025-IMO), E_g results to be 2.8 eV: Fe-doped IMO is approaching the behaviour of a semiconductor, confirming, at least qualitatively, the previous hypothesis (Alvarez-Ramírez 2009) that the presence of iron could modify the conduction properties of IMO (an electrical insulator). With Fe-L-IMO, a further reduction of the bandgap could be observed ($E_g = 2.4$ eV); however, a precise determination of the bandgap is hampered by the presence of Fe_2O_3 clusters along with substitutional iron.

To elicit further information about the natures of different Fe^{3+} species, EPR spectroscopy was used to study both Fe-0.025-IMO and Fe-L-IMO samples, namely, the sample carrying mostly isolated Oh Fe^{3+} sites and the sample with the highest amount of clusters, respectively. Figure 11 shows EPR spectra of fresh samples, which are dominated by an absorption feature at $g_{eff} = 4.3$ and two broad lines, largely superimposed, at $g_{eff} \cong 2.0$ and 2.3. In aluminium silicates, Fe^{3+} is usually present in high-spin ferric state ($S = 5/2$), consistently with the weak ligand field provided by possible ligands (water, hydroxide or oxide ions). Under those circumstances, the X-band (~ 9 –10 GHz) EPR spectrum usually consists of a prominent peak at $g_{eff} = 4.3$ and possible other broader peaks down to $g_{eff} \cong 9$, where g_{eff} is an effective g factor, phenomenologically accounting for the fact that, at this frequency, EPR transitions only occur within doublet states and not between them (Pilbrow 1990). The $g_{eff} = 4.3$ line observed in Fig. 11a is assigned to the presence of isolated Fe^{3+} ions in high-spin state, likely corresponding to species absorbing at 270 nm in the DR-UV–Vis spectra. The relative intensity of the $g_{eff} = 4.3$ line is slightly higher with Fe-0.025-IMO, the sample at lower Fe loading, in agreement with other authors (Goldfarb et al. 1994). The $g_{eff} \cong 2.0$ and 2.3 lines are usually associated to iron oxide clusters and/or particles where Fe^{3+} ions strongly interact with each other (Goldfarb et al. 1994; Bordiga et al. 1996; Ferretti et al. 2004). Any evaluation of the relative spin concentration of isolated and clustered Fe^{3+} species was hampered, in this case, due to the high anisotropy in the transition probabilities of Fe^{3+} high-spin states: both magnetic susceptibility and UV–Vis measurements, however,

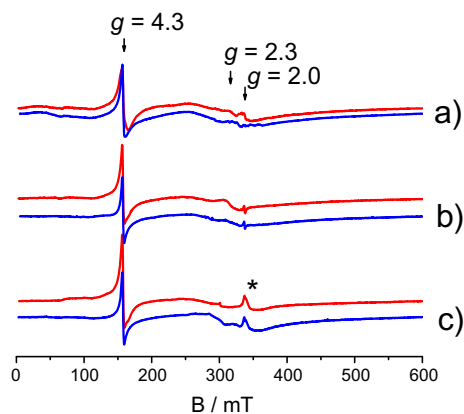


Fig. 11 X-band EPR spectra of Fe-0.025-IMO (red curves) and Fe-L-IMO (blue curves): **a** fresh samples, **b** samples dehydrated for 1 h at 473 K and **c** NO-loaded samples (10 mbar). All spectra were recorded at 77 K. (Color figure online)

showed that isolated Fe^{3+} species are much more abundant in Fe-0.025-IMO.

Upon dehydration of the samples at 473 K (Fig. 11b), the feature at $g_{\text{eff}} = 2.0$ strongly reduces in intensity, while the signal at $g_{\text{eff}} = 2.3$ increases, in particular with Fe-0.025-IMO. A similar behaviour, already reported in iron-loaded zeotype materials, was attributed to the formation of “aggregated” Fe^{3+} species brought about by dehydration (Berlier et al. 2002; Umamaheswari et al. 2006). Assuming the $g_{\text{eff}} = 4.3$ signal to be a marker of structural Fe^{3+} , its intensity remains almost constant in the two samples, despite the different iron contents, indicating that the corresponding sites are rather stable. In order to verify the chemical reactivity of Fe^{3+} species and the possible presence of reduced Fe^{2+} species, 10 mbar of NO was dosed at room temperature on the two dehydrated samples (Fig. 11c): during thermal treatment, reduction from (reactive) Fe^{3+} species to EPR silent Fe^{2+} species was indeed reported for other materials (Joyner and Stockenhuber 1999; Fiscaro et al. 2003). Such Fe^{2+} species readily react with NO to form Fe^{2+} –NO complexes, with total spin $S = 3/2$, which are characterized by distinct EPR signals, dominated by a feature at $g_{\text{eff}} = 4.0$ (Umamaheswari et al. 2006). In the present case, no EPR signal typical for Fe^{2+} –NO complexes was observed in Fig. 11c, indicating that no reduction of Fe^{3+} occurs under the applied treatment, in agreement with the assumption of the framework nature of those sites.

Formation of Fe^{3+} –NO adducts is expected to lead to integer spin states that are not observable at the operational frequency used in this study (9.5 GHz) (Pilbrow 1990). This may explain the disappearance of the $g_{\text{eff}} = 2.3$ upon NO dosage on Fe-0.025-IMO sample. Comparison of the Fe^{3+} signal prior and after NO adsorption (Fig. 10b, c, respectively), however, indicates that no reduction in the overall EPR signal intensity occurs, suggesting that probably such complexes are not formed. This may be explained by considering that the EPR active Fe^{3+} species are coordinatively saturated and not capable to coordinate the NO molecule. Evidence for NO physisorption at strongly polarizing cationic sites is instead provided by a small signal (asterisk in Fig. 11c), typical for NO molecules adsorbed on Al^{3+} sites in aluminosilicate zeotype materials (Pöpple et al. 2004; Lunsford 1968).

Conclusion

The two possible fates for Fe^{3+} cations in contact with IMO systems, either IS to isolated Oh Fe^{3+} species or clustering to Fe oxides, depend more on the Fe amount rather than the preparation route. Evidence is provided that $\text{Fe}^{3+}/\text{Al}^{3+}$ IS is the major process occurring in the sample at the lowest Fe content produced by direct synthesis. When the amount of Fe is increased, the content in isolated Oh Fe^{3+} species increases up to a limit of 0.9 wt%, in fair agreement with what was observed for Fe-doped aluminium-germanates. The rest forms Fe_2O_3 clusters. Interestingly, when the post-synthesis loading procedure is adopted, the same situation is arrived at, with the same maximum amount of Fe in the IMO structure, and the rest constituting Fe oxide clusters. The only difference between the two cases seems to be the size of clusters (larger with Fe-L-IMO sample) and possibly their phase (hematite vs maghemite), both factors affecting the magnetic properties.

Isolated Oh Fe^{3+} species coming from IS occur in high-spin state: also, their full coordination degree hampers interaction with molecules like NO and are rather stable upon dehydration at 423 K. Mössbauer spectroscopy and EPR ruled out the formation of Fe^{2+} in both fresh and outgassed samples, respectively. Nonetheless, the presence of Fe affects the bandgap of the final material, in that the bandgap of IMO (an electrical insulator) is decreased.

Room-temperature magnetic susceptibility measurements indicate that IMO NTs have a diamagnetic response, as expected, whereas all Fe-doped samples display a dominant paramagnetic behaviour. In Fe-0.025-IMO, the agreement between theoretical prediction and experimental data for the χ_{para} indicates that the paramagnetic signal entirely comes from isolated Fe^{3+} ions; in both Fe-0.050-IMO and Fe-L-IMO samples, these measurements point to a lower-than-expected content of isolated Fe^{3+} ions, in agreement with UV–Vis spectroscopy indicating the presence of Fe_2O_3 clusters. The magnetic moments in Fe_2O_3 clusters are presumed to be highly disordered because of the pinning effect of a strong, random surface anisotropy; the sigmoidal magnetic signal basically arises from partial field-induced unpinning of a fraction of moments.

The IMO structure so appears able to exchange dynamically with water solution Al and Fe ions. This

fact indicates that ionic exchange is a viable method to introduce heteroatoms at the outer surface of IMO NTs, avoiding more complicated synthesis procedures. Besides Fe^{3+} , other metals with suitable charge and dimensions could be hosted at the outer surface of IMO NTs, including Cr^{3+} and Ti^{3+} , for instance. This result is of particular interest, since Fe-doped IMO NTs could be useful for applications involving materials with both high porosity, high surface area and the presence of accessible transition metals, including adsorption and catalysis.

References

- Ackerman WC, Smith DM, Huling JC, Kim Y, Bailey JK, Brinker CJ (1993) Gas/vapor adsorption in imogolite: a microporous tubular aluminosilicate. *Langmuir* 9:1051–1057
- Alvarez-Ramírez F (2009) First principles studies of Fe-containing aluminosilicate and aluminogermanate nanotubes. *J Chem Theory Comput* 5:3224–3231
- Amara MS, Rouzière S, Paineau E, Bacia-Verloop M, Thill A, Launois P (2014) Hexagonalization of aluminogermanate imogolite nanotubes organized into closed-packed bundles. *J Chem Phys C* 118:9299–9306
- Arancibia-Miranda N, Escudey M, Pizarro C, Denardin JC, García-González MT, Fabris JD, Charlet L (2014) Preparation and characterization of a single-walled aluminosilicate nanotube-iron oxide composite: its applications to removal of aqueous arsenate. *Mater Res Bull* 51:145–152
- Avellan A, Levard C, Kumar N, Rose J, Olivi L, Thill A, Chaurand P, Borschneck D, Masion A (2014) Structural incorporation of iron into Ge-imogolite nanotubes: a promising step for innovating nanomaterials. *RSC Adv* 4:49827–49830
- Berlier G, Spoto G, Bordiga S, Ricchiardi G, Fiscaro P, Zecchina A, Rossetti I, Selli E, Forni L, Giamello E, Lamberti C (2002) Evolution of extraframework Iron species in Fe silicalite: 1. Effect of Fe content, activation temperature, and interaction with redox agents. *J Catal* 208:64–82
- Bonelli B, Bottero I, Ballarín N, Passeri S, Cavani F, Garrone E (2009) IR spectroscopic and catalytic characterization of the acidity of imogolite-based systems. *J Catal* 264:15–30
- Bonelli B, Armandi M, Garrone E (2013) Surface properties of aluminosilicate single-walled nanotubes of the imogolite type. *Phys Chem Chem Phys* 15:13381–13390
- Bordiga S, Buzzoni R, Geobaldo F, Lamberti C, Giamello E, Zecchina A, Leofanti G, Petrini G, Tozzola G, Vlaic G (1996) Structure and reactivity of framework and extraframework iron in Fe-silicalite as investigated by spectroscopic and physicochemical methods. *J Catal* 158:486–501
- Borghi E, Occhiuzzi M, Foresti E, Lesci IG, Roveri N (2010) Spectroscopic characterization of Fe-doped synthetic chrysotile by EPR, DRS and magnetic susceptibility measurements. *Phys Chem Chem Phys* 12:227–238
- Bottero I, Bonelli B, Ashbrook S, Wright P, Zhou W, Tagliabue M, Armandi M, Garrone E (2011) Synthesis and characterization of hybrid organic/inorganic nanotubes of the imogolite type and their behaviour towards methane adsorption. *Phys Chem Chem Phys* 13:744–750
- Chikazumi S (1997) *Physics of ferromagnetism*, 1997th edn. Oxford University Press, Oxford. ISBN 0-19-851776-9
- Coe JMD (2009) *Magnetism and magnetic material*. Cambridge University Press, Cambridge. ISBN 9780521816144
- Cradwick PDG, Farmer VC, Russell JD, Wada K, Yoshinaga N (1972) Imogolite, a hydrated aluminium silicate of tubular structure. *Nat Phys Sci* 240:187–189
- Eid C, Luneau D, Salles V, Asmar R, Monteil Y, Khoury A, Brioude A (2011) Magnetic properties of hematite nanotubes elaborated by electrospinning process. *J Phys Chem C* 115:17643–17646
- Fallet M, Gschwind R, Bauer P (2003) Oxidation states of iron in doped $\text{TiO}_2\text{-SiO}_2$ sol-gel powders: a ^{57}Fe Mössbauer study. *J Sol Gel Sci Technol* 27:167–173
- Farmer VC, Fraser AR (1978) Synthetic imogolite: a tubular hydroxylaluminium silicate. In: *Proceedings of the international clay conference*. Elsevier, Amsterdam, pp 547–554
- Farmer VC, Adams MJ, Fraser AR, Palmieri F (1983) Synthetic imogolite: properties, synthesis, and possible applications. *Clay Miner* 18:459–472
- Ferretti AM, Barra AL, Forni L, Oliva C, Schweiger A, Ponti A (2004) Electron paramagnetic resonance spectroscopy of iron(III)-doped mfi zeolite. 1. Multi-frequency CW-EPR. *J Phys Chem B* 108:1999–2005
- Fiscaro P, Giamello E, Berlier G, Lamberti C (2003) Paramagnetic nitrosyliron adducts in pentasilic zeolites: an EPR study. *Res Chem Intermed* 29:805–816
- Goldfarb D, Bernardo M, Stoheimer KG, Vaughan DEW, Tomann H (1994) Characterization of iron in zeolites by X-band and Q-band ESR, pulsed ESR, and UV-Visible spectroscopies. *J Am Chem Soc* 116:6344–6353
- Joyner RW, Stockenhuber M (1999) Preparation, characterization, and performance of Fe-ZSM-5 catalysts. *J Phys Chem B* 103:5963–5976
- Kang D-Y, Zang J, Jones CW, Nair S (2011) Single-walled aluminosilicate nanotubes with organic-modified interiors. *J Phys Chem C* 115:7676–7685
- Kang D-Y, Brunelli NA, Yucelen GI, Venkatasubramanian A, Zang J, Leisen J, Hesketh PJ, Jones CW, Nair S (2014) Direct synthesis of aminoaluminosilicate nanotubes with enhanced molecular adsorption selectivity. *Nat Commun* 5:3342
- Kodama RH, Berkowitz AE, McNiff EJ, Foner S (1996) Surface spin disorder in NiFe_2O_4 nanoparticles. *Phys Rev Lett* 77:394–397
- Konduri S, Mukherjee S, Nair S (2006) Strain energy minimum and vibrational properties of single-walled aluminosilicate nanotubes. *Phys Rev B* 74:033401
- Lopez T, Moreno JA, Gomez R, Bokhimi X, Wang JA, Yee-Madeira H, Pecchi G, Reyes P (2002) Characterization of iron-doped titania sol-gel materials. *J Mater Chem* 12:714–718
- Lunsford JH (1968) Surface interactions of NaY and decationated Y zeolites with nitric oxide as determined by electron paramagnetic resonance spectroscopy. *J Phys Chem* 72:4163–4168

- MacKenzie KJ, Bowden ME, Brown JWM, Meinhold RH (1989) Structure and thermal transformations of imogolite studied by ^{29}Si and ^{27}Al high-resolution solid-state nuclear magnetic resonance. *Clay Clay Miner* 37:317–324
- Mukherjee S, Bartlow VM, Nair S (2005) Phenomenology of the growth of single-walled aluminosilicate and aluminogermanate nanotubes of precise dimensions. *Chem Mater* 17:4900–4909
- Ookawa M (2012) Synthesis and characterization of Fe-Imogolite as an oxidation catalyst. In: *Clay minerals in nature—their characterization, modification and application*. InTech, pp 239–257. ISBN 978-953-51-0738-5
- Ookawa M, Inoue Y, Watanabe M, Suzuki M, Yamaguchi T (2006) Synthesis and characterization of Fe containing imogolite. *Clay Sci* 12:280–284
- Papaefthymiou GC, Bustamante A, Scorzelli RB (2002) Mössbauer characterization of iron oxide nanoclusters grown within aluminosilicate matrices. *MRS Proc* 746(R5):1. doi:[10.1557/PROC-746-R5.1](https://doi.org/10.1557/PROC-746-R5.1)
- Pilbrow JR (1990) Transition ion electron paramagnetic resonance. Clarendon Press, Oxford. ISBN 0-198-55214-9
- Pöpple A, Gutjahr M, Rudolf T (2004) Molecules in interaction with surfaces and interfaces, vol 634., *Lect Notes Phys*-Springer, Berlin, p 185. ISBN 978-3-540-40024-0
- Reis STD, Pontuschka WM, Yang JB, Faria DLA (2003) Properties and structural features of Fe doped BABAL glasses. *Mat Res* 6:389–394
- Thill A, Maillet P, Guiose B, Spalla O, Belloni L, Chaurand P, Auffan M, Olivi L, Rose J (2012) Physico-chemical control over the single- or double-wall structure of aluminogermanate imogolite-like nanotubes. *J Am Chem Soc* 134:3780–3786
- Umamaheswari V, Böhlmann W, Pöppel A, Vinu A, Hartmann M (2006) Spectroscopic characterization of iron-containing MCM-58. *Microporous Mesoporous Mater* 89:47–57
- Wada SI (1987) Imogolite synthesis at 25 & #xB0;C. *Clay Miner* 35:379–384
- Wada SI, Eto A, Wada K (1979) Synthetic allophane and imogolite. *J Soil Sci* 30:347–355
- Wang Y, Zhang QH, Shishido T, Takehira K (2002) Characterization of iron-containing MCM-41 and its catalytic properties in epoxidation of styrene with hydrogen peroxide. *J Catal* 209:186–196
- Wilson MA, Lee GSH, Taylor RC (2002) Benzene displacement on imogolite. *Clays Clay Miner* 50:348–351
- Yoshinaga N, Aomine A (1962) Imogolite in some Ando Soils. *Soil Sci Plant Nutr* 8:22–29
- Zanzottera C, Vicente A, Armandi M, Fernandez C, Garrone E, Bonelli B (2012) Thermal collapse of single-walled aluminosilicate nanotubes: transformation mechanisms and morphology of the resulting lamellar phases. *J Phys Chem C* 116:23577–23584
- Zysler RD, De Biasi E, Ramos CA, Fiorani D, Romero H (2005) Surface and interparticle effects in amorphous magnetic nanoparticles. In: Fiorani D (ed) *Surface effects in magnetic nanoparticles*. Springer Science + Business Media, New York, pp 239–261